Journal of Magnetism and Magnetic Materials 471 (2019) 486–494

Contents lists available at ScienceDirect

Journal of Magnetism and Magnetic Materials

journal homepage: www.elsevier.com/locate/jmmm

Research articles

Heating efficiency of magnetic nanoparticles decreases with gradual immobilization in hydrogels

Ulrich M. Engelmann[a,1,*], Julian Seifert[b,1], Benedikt Mues[a], Stefan Roitsch[b], Christine Ménager[c], Annette M. Schmidt[b], Ioana Slabu[a,*]

[a] Applied Medical Engineering, Helmholtz Institute, Medical Faculty, RWTH Aachen University, 52074 Aachen, Germany
[b] Institute of Physical Chemistry, Universität zu Köln, 50939 Köln, Germany
[c] Université Pierre et Marie Curie, UPMC-Univ Paris 06, Laboratoire PECSA-UMR 7195-CNRS-ESPCI, 75252 Paris, France

ARTICLE INFO

Keywords:
Magnetic nanoparticles
Magnetic fluid hyperthermia
Ferrohydrogels
Phantom tissue gels
Particle immobilization

ABSTRACT

Magnetic nanoparticles (MNP) applied in magnetic fluid hyperthermia cancer treatment interact with cancerous tissue in various ways. The impact of these interactions on MNP heating efficiency is hard to quantify and strongly depends on the MNP mobility inside the cancerous environment. There, this MNP mobility is inhibited by cell attachment and internalization. In this study, we model this impact and analyze the MNP heating under gradual immobilization of MNP in acrylamide hydrogels with tailored mesh size. Our results confirm a clear particle heating dependency on the state of immobilization of MNP. This state is related to the mean mesh size of the respective hydrogel. From this, the contributions of Brownian and Néel relaxation mechanisms to the overall particle heating are estimated. In fact, the heating efficiency decreases by up to 35% for the highest immobilization state of MNP. This result is discussed in the context of the field-dependent Brownian and Néel relaxation time, showing that the former significantly contributes to the heating efficiency even for small particles under the field parameters employed in this study.

1. Introduction

Magnetic Nanoparticles (MNP) generate heat when subjected to an alternating magnetic field (AMF) [1,2]. Such heat can be locally delivered at a target site, e. g. a tumor, and be used therapeutically for hyperthermic tumor destruction [3,4] or as an adjunct in chemotherapy [5,6] or radiation therapy [7,8]. The local delivery of heat via MNP is known as magnetic fluid hyperthermia (MFH) and has been successfully applied to glioblastoma brain tumors and prostate tumors in clinical trials within the last decade [7,9]. Generally, cell death is induced at temperatures higher than 43 °C for treatment durations longer than 10 min [2,10]. Usually, solutions containing freely dispersed MNP easily develop such high temperatures when they are exposed to an AMF. In this case, both the Néel and the Brownian relaxation mechanisms contribute to the overall heating of the MNP solution. However, MNP are immobilized in a tumor environment as they inevitably interact with cells, attach and agglomerate at the cell membrane from where they are internalized into lysosomes [11,12]. Such intracellular MNP generate much less heat compared to MNP freely dispersed in water [13] or cell medium [14]. Concerning this issue, it was recently shown that the inhibition of physical Brownian particle rotation upon MNP immobilization is the dominating factor for the observed decrease in heating [15].

To study the effect of particle immobilization in human tissue, hydrogels offer versatile possibilities to design tissue-equivalent phantoms due to their biocompatibility, mechanical properties and especially their tunable mesh sizes [16,17]. The incorporation of MNP into hydrogels leads to magnetically manipulable hybrid structures, so called ferrohydrogels, with tunable properties depending on the crosslinking density and softness of the hydrogel on the one hand, and on the shape and magnetic properties of the MNP on the other hand. These ferrohydrogels offer promising possibilities in materials analysis and in biomedical applications: Hydrogel-entrapped MNP can be used as magneto-mechanical probes to non-invasively analyze the mechanic properties of hydrogel networks [18]. Further, the deformation of ferrohydrogels in magnetic field gradients has been exploited to design remote controlled drug and cell delivery systems [19]. Due to their tunable heating properties, ferrohydrogels were also used for MFH in tumor therapy [20] and thermosensitive drug delivery [21].

In the present study, we investigate the effect of gradual

* Corresponding authors at: Applied Medical Engineering (Helmholtz-Institute), RWTH Aachen University, Pauwelsstrasse 20, 52072 Aachen, Germany.
E-mail addresses: engelmann@ame.rwth-aachen.de (U.M. Engelmann), slabu@ame.rwth-aachen.de (I. Slabu).
[1] These authors contributed equally to this work and share first authorship.

https://doi.org/10.1016/j.jmmm.2018.09.113
Received 24 June 2018; Received in revised form 26 September 2018; Accepted 28 September 2018
Available online 29 September 2018

immobilization of MNP on their heating efficiency. Therefore, polyacrylamide ferrohydrogels with tailored mesh sizes in the range of the hydrodynamic size of the MNP are synthesized. The MNP are incorporated inside these gels. The mean mesh size of the hydrogels is determined from rheological measurements. The MNP characterization is performed with transmission electron microscopy (TEM), dynamic light scattering (DLS) and SQUID magnetometry. From the heating measurements we estimate the contribution of Brownian particle relaxation to MNP heating and discuss its dependence on the field parameters employed in this study.

2. Material and methods

2.1. Particle synthesis and characterization

Iron-oxide MNP were synthesized via alkaline co-precipitation of $FeCl_2$ and $FeCl_3$ salts in NH_3 aq. (20%), according to the procedure of Massart [22], and coated with sodium citrate, as previously reported in [23].

Transmission electron microscopy (TEM) characterization of MNP samples was conducted with a Zeiss LEO 906 TEM (Carl Zeiss GmbH, Oberkochen, Germany) operated at 60 kV. Before each measurement, 1 µL sample was dried on Cu/Rh-150 maxtaform-grids (Electron Microscopy Sciences, Hatfield, PA, USA) for one hour. Particle core diameters (d_C) were determined from TEM images by manual measurement employing the software PaintNET [24]. The resulting values were fitted with the cumulative distribution function (CDF) of the log-normal distribution probability density function (s. Appendix A).

The MNP hydrodynamic size was characterized by dynamic light scattering (DLS) with a Zetasizer Nano S (Malvern Instruments Ltd., Worcestershire, UK). For that, 500 µL MNP solution diluted to an iron concentration of 1.2 µg(Fe)/mL was measured at 293.15 K at a back-scattering angle of 173° and the procedure was repeated in triplicate The average hydrodynamic diameter was determined from fitting the log-normal distribution probability density function (PDF) (s. Appendix A) to the intensity-weighted MNP hydrodynamic size distribution.

For the MNP magnetic characterization, superconducting quantum interference device (SQUID) magnetometry was carried out with a Magnetic Properties Measurement System (MPMS; Quantum Design Inc., San Diego, CA, USA) operated at 295 K. For this, 60 µL MNP samples containing 6.5 wt-% mannitol were freeze-dried in 100 µL polycarbonate capsules (Quantum Design Inc.). The magnetization, $M(H)$, was measured varying the magnetic field from $-4000\ \mathrm{kA{\cdot}m^{-1}}$ to $4000\ \mathrm{kA{\cdot}m^{-1}}$. The resulting $M(H)$ data was normalized to the absolute amount of iron per sample and fitted with the Langevin function $M(H) = M_S(\coth(z) - 1/z)$, with $z = (\xi - \xi_0)/s$, $\xi = \mu_0 M_S V_C H/(k_B T)$, $V_C = \pi/6 \cdot d_C^3$ the MNP core volume and $\mu_0 = 4\pi \cdot 10^{-7}\ \mathrm{VsA^{-1}m^{-1}}$ the vacuum magnetic permeability. Furthermore, zero-field-cooled field-cooled (ZFC-FC) measurements were performed on the same batch of particles varying the temperature from 5 K to 295 K at constant magnetic field of $0.8\ \mathrm{kA{\cdot}m^{-1}}$. The ZFC-FC curves were normalized to the saturation magnetization M_S derived from fitting the Langevin function to the $M(H)$ data.

2.2. Hydrogel synthesis and characterization

Acrylamide (Aam, ≥99%), N,N′-methylenebisacrylamide (BIS, 99%), N,N,N′,N′-tetramethylethylene-diamine (TEMED, 99%) and ammonium persulfate (APS, ≥98%) were purchased from Sigma-Aldrich.

For the preparation of hydrogels, Aam and the crosslinker BIS were dissolved in deionized water (DI-H_2O) at a volume fraction of $\nu_{pol} = 0.08 = ((m_{Aam} + m_{BIS})/\rho_{PAam})/(m_{tot}/\rho_{H2O})$, with $\rho_{PAam} = 1.3\ \mathrm{g{\cdot}cm^{-3}}$ and $\rho_{H2O} = 1.0\ \mathrm{g{\cdot}cm^{-3}}$ the density of polyacrylamide and water, respectively, and m_{Aam}, m_{BIS} and m_{tot} denoting the masses of Aam, BIS and the total solution mass. The crosslinking degree for different hydrogels was adjusted by variation of the crosslinker mole fraction $\alpha = n_{BIS}/(n_{BIS} + n_{Aam})$ between $\alpha = 0$ and $\alpha = 0.005$ (s. Supplementary Material S3 for further details). The free radical polymerization was initialized by adding APS with a mass fraction of $\mu_m = 0.002$ and TEMED to the polymer solution. After mixing all components in a glass vial, the mixture was transferred to a cylindrical Teflon mold (diameter $d = 40$ mm, volume $V = 2.6$ mL) and was kept for polymerization at room temperature for at least 1 h. Then, the resulting gel was carefully removed from the mold.

Rheological measurements were performed using an AR-G2 rheometer (TA Instruments, New Castle, DE, USA) with a plate-plate geometry ($d = 40$ mm). A solvent trap filled with DI-H_2O was used to adjust the water vapor pressure and prevent solvent evaporation from the hydrogel. Strain sweep experiments were performed at a frequency of 1 Hz in the strain regime $0.0002 \leq \gamma \leq 0.02$. Frequency sweep experiments in the range of 0.1–100 Hz were carried out in the linear viscoelastic regime at a constant strain of 0.002. From these measurements, the frequency dependent storage modulus, G', and loss modulus, G'', of the hydrogels are determined.

Vibrating sample magnetometry (VSM) measurements were conducted on ferrohydrogel samples employing a EV 7 vibrating sample magnetometer (MicroSense, Lowell, MA, USA) operated at $T = 300$ K with a magnetic field ranging from $-1430\ \mathrm{kA{\cdot}m^{-1}}$ to $1430\ \mathrm{kA{\cdot}m^{-1}}$. Ferrohydrogel samples were prepared as described above in cylindrical teflon moulds with a volume of approximately 55 µL with $\nu_{pol} = 0.08$ and various crosslinker mole fractions ranging from $\alpha = 0.0005$ to $\alpha = 0.005$. The MNPs were added as suspension in water (partially replacing water added for gel synthesis) to achieve a final MNP concentration of 300 µg(Fe)/mL. As a reference sample a dispersion of MNP in water was measured.

TEM images of freeze-fractured, freeze-dried ferrohydrogel samples were acquired with a Zeiss LEO 912 Omega (Carl Zeiss). For that, 55 µL ferrohydrogel ($\nu_{pol} = 0.08$, $\alpha = 0.00075$) with an iron concentration of 300 µg(Fe)/mL was frozen in liquid nitrogen, finely ground and placed onto a copper grid with a carbon-hole film (Quantifoil® Multi A, Quantifoil Micro Tools GmbH, Großlöbichau, Germany). The ferrohydrogel on the copper grid was freeze-dried in a VTR 5036 vacuum drying oven (Heraeus Holding GmbH, Hanau, Germany) overnight.

2.3. Calorimetric particle heating measurements

Calorimetric particle heating measurements were carried out with a custom-built hyperthermia setup (Trumpf Hüttinger, Freiburg, Germany), consisting of a DC generator, an AC-resonant oscillator and a water-cooled copper coil. The field amplitude, H_0, and the frequency, f, were set to $H_0 = 40\ \mathrm{kA{\cdot}m^{-1}}$ and $f = 270$ kHz. 1 mL samples were prepared in 4 mL glass vials, which were wrapped in 1 mm thick Styrofoam to reduce heat losses and placed in the 7-turn coil (s. Supplementary Materials S1 for further details on the setup). Samples were exposed to the alternating magnetic field for 30 min starting at an initial temperature of $T_0 = 308.15$ K (35 °C). During exposure, the sample temperature was recorded with a fiber-optic thermometer Luxtron 812 (LumaSense Inc., Santa Barbara, CA, USA). Sample heating curves are shown in the Supplementary Material S2. The measured temperature-time data, $T(t)$, were fitted with the Box-Lucas function

$$T(t) = T_{rise} \cdot (1 - \exp(-\frac{t}{\tau})) + T_0 \quad (1)$$

from which the specific absorption rate (SAR) value was calculated according to [25]:

$$\mathrm{SAR} = \frac{c}{\rho} \cdot \frac{\mathrm{d}T}{\mathrm{d}t}|_{t \to 0} \quad (2)$$

with the specific heat capacity of water, $\boldsymbol{c} = 4.187\ \mathrm{J\ (g{\cdot}K)^{-1}}$, the MNP weight fraction, $\boldsymbol{\rho}$, and $\mathrm{d}T/\mathrm{d}t|(t \to 0) = \frac{T_{rise}}{\tau}$, derived from the Box-Lucas fitting parameters.

Ferrohydrogel samples were prepared as described above (cf.

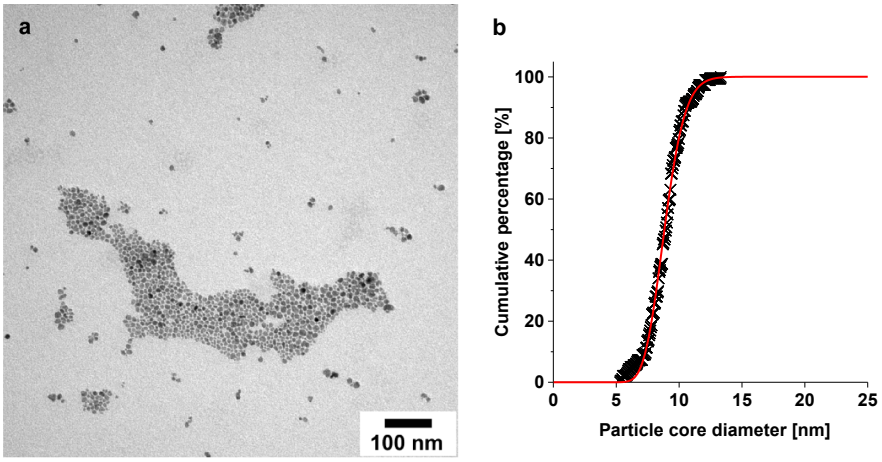

Fig. 1. (a) Exemplary transmission electron microscopy (TEM) image of MNP. (b) Particle core diameter distribution derived from TEM images for N = 755 particles (crosses) with fit to the cumulative distribution function of the log-normal distribution (red line) (R^2 = 0.999) yielding d_C = (8.9 ± 1.3) nm with a log-normal distribution width of σ = 0.146. (For interpretation of the references to colour in this figure legend, the reader is referred to the web version of this article.)

Section 2.2) with the difference that a solution with MNP suspended in DI-H_2O was used instead of water. The final MNP mass in each 1 mL sample was 300 μg(Fe). Further reference measurements were performed on MNP dispersed in water and on hydrogels without MNP, which served for comparison and background subtraction, respectively.

3. Results and discussion

3.1. Particle characterization

Characterization via TEM analysis yields a log-normal distributed particle size with a mean core diameter of d_C = (8.9 ± 1.3) nm with a log-normal distribution width of σ= 0.146 (Fig. 1). The narrow size distribution of the MNP demonstrates the monodisperse character of the MNP. The MNP size reported here is in very good agreement with the one reported previously for MNP synthesized with the same protocol [23].

The hydrodynamic diameter investigated via DLS results in d_H=(18.9±6.1) nm (Fig. 2).

The magnetization curve from SQUID magnetometry normalized to the absolute amount of iron oxide per sample yields a saturation magnetization M_S=(445.9±7.1) kA·m^{-1} (Fig. 3a), which is about 93% of bulk magnetite magnetization M_S^{bulk}= 476 kA·m^{-1} [26]. Generally, a lower-than-bulk M_S is expected for MNP caused by a magnetic dead layer that consists of canted spins at the particle surface, which do not contribute to the overall MNP magnetization [27]. Nevertheless, it was recently shown that high magnetic field up to 4000 kA·m^{-1} can even align these canted surface spins [28]. As our magnetization curve is measured in the same field range, such an effect could explain the high saturation values close to bulk value as observed here.

ZFC-FC measurements on the same batch of particles show a peak temperature in the ZFC-curve at T_{max}≈ 87 K (Fig. 3b). Using the relation $25 \cdot k_B T_{max} = K_{eff} \cdot V_C$ [29], we estimate an effective anisotropy constant of K_{eff}= 81 kJ·m^{-3}, which is in line with the value reported in a previous study for MNP synthesized with the same protocol [13].

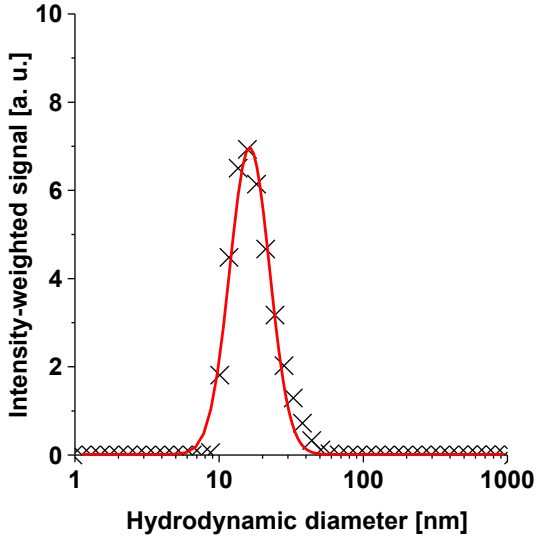

Fig. 2. Intensity size distribution of the hydrodynamic diameter of MNP (crosses) with a fit to the PDF of a log-normal distribution (red line) (R^2= 0.979) yielding d_H= (18.9 ± 6.1) nm.

3.2. Hydrogel characterization

3.2.1. Rheological characterization and determination of mesh sizes

The frequency dependent storage modulus, G', and loss modulus, G'', of hydrogels are determined by oscillatory shear experiments as described above (cf. Section 2.2). Exemplary data for selected hydrogels is shown in Fig. 4. For all hydrogels analyzed in this work, G', representing the energy density stored by mechanic deformation, is significantly higher than G'', which denotes the energy density dissipated by viscos flow, indicating essentially elastic behavior of the hydrogels.

The moderate increase of the storage modulus, G', with frequency allows an estimation of the plateau storage modulus, $G_P^{'}$, by averaging in the frequency regime 0.1–10 Hz [30]. In rubber elasticity theory, the equilibrium shear modulus, G, of the hydrogel is connected to number of elastically active polymer chains per unit volume, n_{el}. For the hydrogels analyzed here, G is identified with the frequency-averaged plateau modulus $G_P^{'}$, and according to the affine network model the following expression is obtained [31–33]:

$$G_P^{'} \approx G = n_{el} k_B T \quad (3)$$

with k_B the Boltzmann constant and T the temperature (here room temperature: 298.15 K). For ideal networks, n_{el} is connected with the number of elastically active crosslinks per unit volume, μ_{el}, by the crosslinker functionality, f', (= 4 for in the case of BIS), according to $\mu_{el} = 2/f' \cdot n_{el}$ [32]. The mesh size of the hydrogel, represented by the distance between two elastically active crosslinks, d_{cross}, is calculated by:

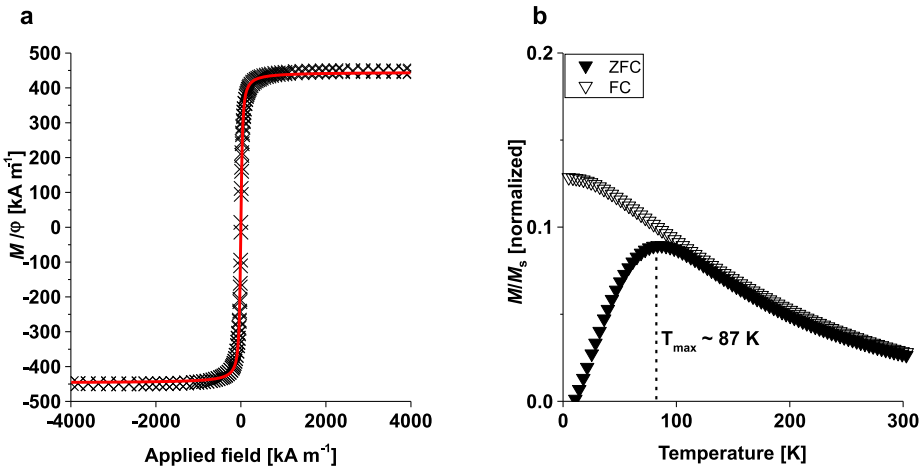

Fig. 3. Magnetic properties of freeze-dried MNP immobilized in mannitol. (a) Magnetization curve (M) normalized to the iron oxide amount (ϕ) (crosses) and Langevin fit (red line) (R^2 = 0.999) yielding M_S= (445.9 ± 7.1) kA·m^{-1}. (b) ZFC-FC curves normalized to the saturation magnetization, the peak maximum in the ZFC curve is at T_{max}= 87 K. (For interpretation of the references to colour in this figure legend, the reader is referred to the web version of this article.)

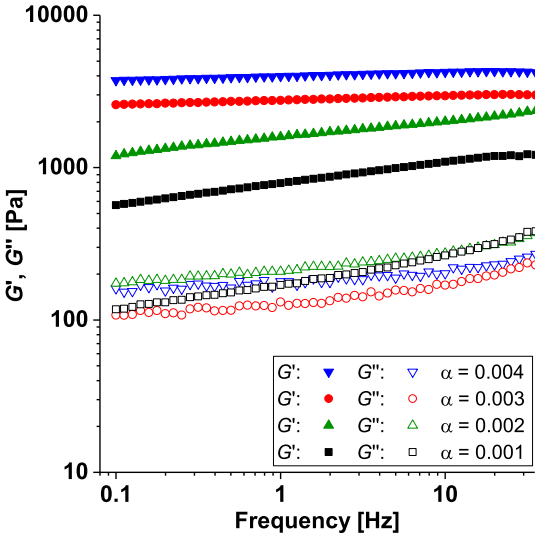

Fig. 4. Frequency-dependent storage G' (solid symbols) and loss moduli G'' (open symbols) measured at a constant strain of γ= 0.002 for hydrogels with ν_{pol}= 0.08 and various crosslinker mole fractions α.

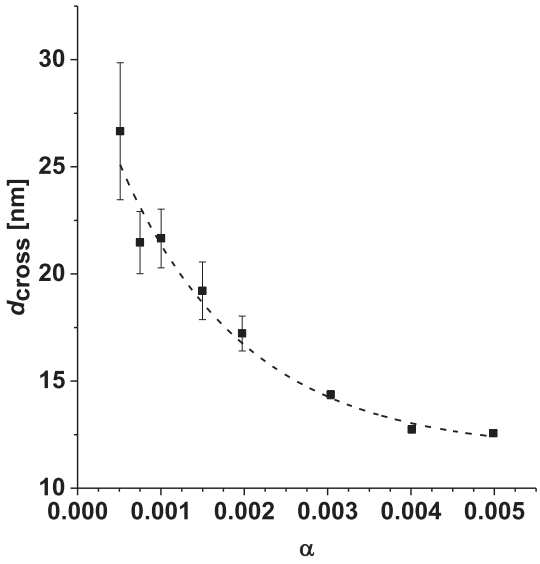

Fig. 5. Mean mesh size d_{cross}, representing the distance between two elastically active crosslinks, in dependence of the crosslinker mole fraction α of the hydrogels. Dashed line is a guide to the eye.

$$d_{cross} = \left(\frac{k_B T \cdot f'}{2G_P'} \right)^{1/3} \quad (4)$$

Results of the mean mesh size in dependence of the crosslinker mole fraction of all hydrogels are summarized in Fig. 5 (s. Supplementary Material S3 for a tabular summary).

The polyacrylamide hydrogels can be synthesized with tunable mesh sizes in the range of (12.6±0.2) nm to (26.7±3.3) nm by variation of the crosslinker mole fractions. The precise control over the mesh size of polyacrylamide gels is described in literature before e. g. for polyacrylamide gels used for gel electrophoresis [34]. Wang et al. describe the mesh size of photopolymerized polyacrylamide gels by gel electrophoresis and rheology measurements. For hydrogels synthesized with a slightly lower polymer volume fraction, $\nu_{pol} \approx$ 0.07, and approximately fivefold higher crosslinker mole fraction, $\alpha \approx$ 0.025, they observe a mean mesh size of 6.4 nm [35]. This is in good agreement with our results, and confirms the decrease of the mesh size with increasing crosslinker mole fraction.

3.2.2. VSM characterization of ferrohydrogels

The normalized magnetization, M/M_s, curves of MNP inside PAAm hydrogels are similar (Fig. 6). Only at low fields the M/M_s values differ from the ones of MNP dispersed in water showing the highest M/M_s. Magnetization values gradually decrease with increasing crosslinker mole fraction α. Such decrease is attributed to a gradual MNP immobilization inside the hydrogels: MNP are gradually inhibited with increasing α in their free physical rotation, which at low fields significantly contributes to the full alignment of the MNP magnetic moments in the direction of the applied field [36]. At low fields, the intrinsic Néel relaxation of MNP is dominated by anisotropy, and the MNP magnetic moment mainly aligns with the applied field by physical rotation. Therefore, MNP in liquid suspension (water and polymer solution) show a higher initial magnetization at low fields compared to MNP immobilized in hydrogels.

3.2.3. TEM characterization of ferrohydrogels

The particle distribution and the network morphology of freeze-fractured, freeze-dried ferrohydrogels are analyzed by direct imaging TEM (Fig. 7). In all investigated gels it was observed that the particles are homogenously distributed inside the hydrogel sample. Particle agglomerates or deformations of the hydrogel matrix in the vicinity of the

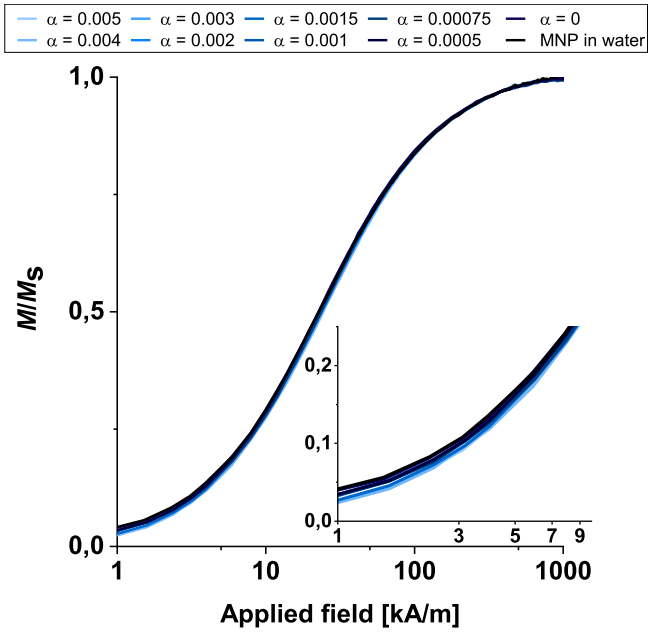

Fig. 6. Normalized magnetization, M/Ms, of MNP immobilized in ferrohydrogels (ν_{pol}= 0.08) for various crosslinker mole fractions. Virgin curves for MNP diluted in polymer solution (without crosslinker BIS added, α= 0) and water are also displayed.

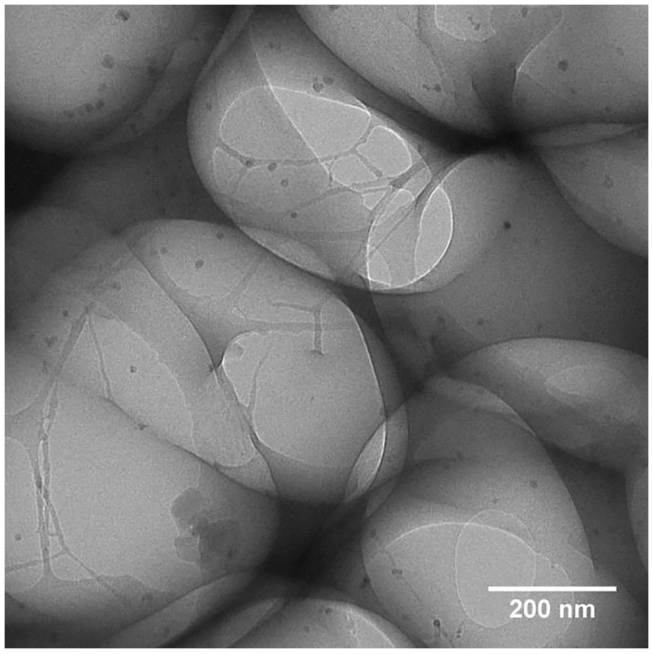

Fig. 7. TEM image of a freeze-dried ferrohydrogel (ν_{pol}= 0.08, α= 0.00075). MNP (visible as dark gray spots) are homogeneously distributed inside the polyacrylamide network.

particles are not observed throughout all gels. The polymer phase consists of strands and layers, which are arranged to a porous structure.

3.3. Particle heating efficiency in hydrogels

3.3.1. Results of particle heating efficiency in hydrogels

We gradually immobilize MNP in mesh size-tunable polyacrylamide hydrogels (cf. Section 3.2 above) and measure the particle heating. The SAR values in dependence of the mean mesh size are summarized in Fig. 8a, normalized to the SAR value of MNP suspended in DI-H_2O

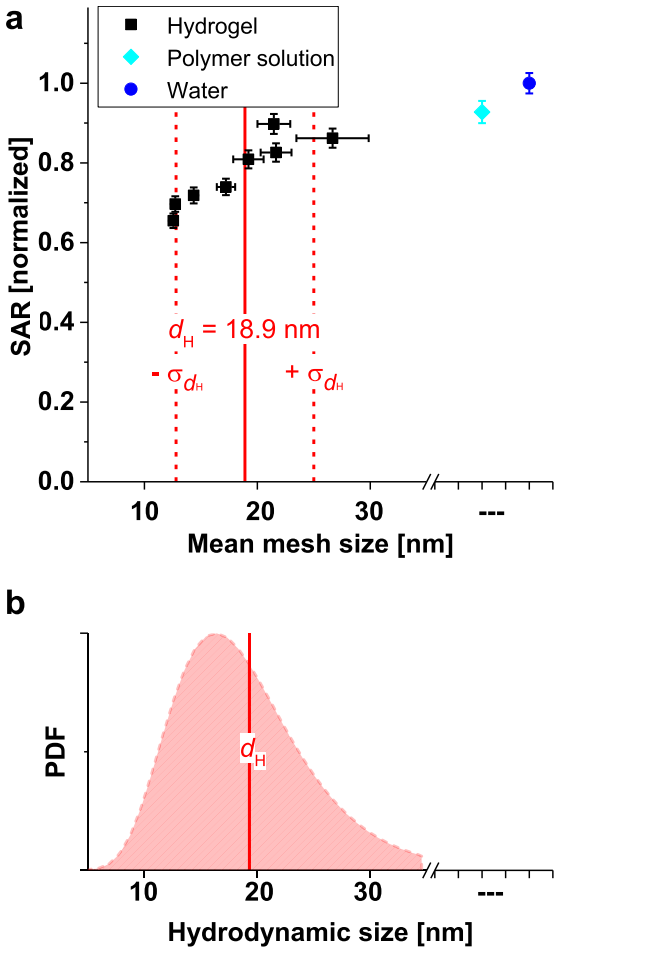

Fig. 8. (a) Normalized SAR values of MNP gradually immobilized in hydrogels with decreasing mean mesh size. SAR values of MNP diluted in polymer solution (without crosslinker BIS added, α= 0) and water are also displayed. The hydrodynamic diameter d_H=(18.9±6.1) nm is denoted with a solid red line, while the region of one standard deviation marked in dashed red lines. (b) Probability density function (PDF) of the log-normal distribution of the hydrodynamic diameters. (For interpretation of the references to colour in this figure legend, the reader is referred to the web version of this article.)

((343±7) W·g^{-1}(Fe)).

The SAR value decreases slightly by 7.3% for MNP suspended in the polymer solution (α= 0) compared to the SAR of MNP suspended in water. For mean mesh sizes $d > d_H$= 18.9 nm, a decrease in SAR values by 10% to 20% is observed, while for $d < d_H$ the SAR values decrease by up to 35%. In fact, the decrease of SAR values from 10% up to 35% demonstrates the effect of MNP immobilization for mean mesh sizes corresponding to the MNP hydrodynamic diameter within their first size standard deviation, namely for mesh sizes between $d_{cross} = d_H + \sigma_{d_H}$= 25.0 nm down to $d_{cross} = d_H - \sigma_{d_H}$= 12.8 nm.

3.3.2. Heating efficiency decrease with viscosity

The MNP suspension in polyacrylamide solution without crosslinker (α= 0) is a complex (non-Newtonian) fluid with a zero-shear viscosity of η_0= (9.521±0.012) Pa·s, thus four orders of magnitude higher than water ($\eta_{H2O} \approx$ 0.001 Pa·s) (s. Supplementary Material S4 for details).

However, for the translational or rotational diffusion of a nanoscopic particle, it has to be taken into account that the length scales of the polymer in solution must be similar to the characteristic size (e. g. the radius) of the diffusing objects [37,38]. The polymer is typically characterized by the correlation length, Ξ, which is the average distance of one monomer in a polymer chain to the next monomer of another

chain [39,40]. It is well-established that the diffusion behavior of a nanoscopic probe (e. g. MNP), depends on the correlation length that can be estimated from [41]:

$$\Xi = b\cdot\nu_{\mathrm{pol}}^{-\frac{\chi}{3\chi-1}} = C_\infty\cdot\frac{l}{\sin\left(\frac{\theta}{2}\right)}\cdot\nu_{\mathrm{pol}}^{-\frac{\chi}{3\chi-1}}, \tag{5}$$

with b = 1.6 nm the Kuhn length, χ= 0.44 the Flory interaction parameter [32], C_∞= 8.5 the characteristic ratio [42], l= 0.154 nm the length of a C-C single bond and their bond angle θ=109.5° [32]. For semi-dilute aqueous solutions of polyacrylamide in water, b, $C_\infty\chi$ are experimentally accessible constants and l and θ are standard parameters for organic compounds. From equation (5), we estimate a correlation length of Ξ= 51.7 nm for the hydrogels studied here. If the size of a particle in the polymer solution is smaller than the correlation length, the particle diffusion is dominated by the solvent (in our case water) viscosity. Here, the correlation length of the polymer solution is larger than the hydrodynamic diameter of the MNP (d_H= 18.9 nm). Thus, for the MNP in polymer solution, the effective nanoscopic viscosity is close to that of water (the solvent). The slight reduction in the SAR value of 7.3% observed for MNP suspended in polyacrylamide solution is ascribed to a minor deceleration of the physical (Brownian) rotation of the MNP, as a consequence of the solvent-dominated viscosity in the non-Newtonian fluid on the particle scale.

A similar reduction in SAR value by approximately 15% was observed recently by Cabrera et al. for iron oxide nanocubes with 14 nm edge length dispersed in glycerol (macroscopic viscosity $\eta_{gly}\approx$ 0.1 Pa·s) [43]. The authors demonstrate a viscosity induced inhibition of Brownian relaxation accompanied by a reduction of the remanence magnetization, M_R, and the saturation magnetization, M_S, determined from dynamic AC-hysteresis measurements. However, glycerol is a Newtonian fluid, for which the macroscopic and nanoscopic viscosity are identical. An increase in fluid macroscopic viscosity therefore leads directly to an equivalent increase in the nanoscopic viscosity, influencing the physical rotation of the particles. Additionally, the anisotropy energy is significantly higher for the 14 nm edge length nanocubes, resulting in a stronger contribution of Brownian relaxation to particle heating. This might explain why the drop in the SAR value observed by Cabrera et al. is much higher compared to the one of the MNP measured in polymer solution in this work.

3.3.3. Heating efficiency decrease with gradual MNP immobilization

The gradual immobilization of MNP inside the hydrogel allows for quantification of the effect of MNP immobilization on particle heating, which shows a decrease of up to 35% in SAR value for the smallest mean mesh size of (12.6±0.2) nm. We expect that a maximum of 86% of the MNP is immobilized, ascribed to hydrodynamic sizes higher than the smallest gel mesh size investigated here (estimated from the PDF fit, Fig. 8). Therefore, we attribute the observed reduction in SAR value to a strong inhibition of the MNP Brownian rotation. This is in line with the findings of Ludwig et al., which reported a reduction of SAR value by approximately 50% for (12−15) nm iron oxide MNP immobilized in 10% polyvinyl alcohol (PVA) hydrogels [44]. Furthermore, AC-susceptibility measurements confirm the inhibition of Brownian rotation for 12 nm MNP upon immobilization inside cells [45]. Moreover, the SAR value of MNP synthesized with the same protocol as the ones used in this study was previously shown to decrease by up to 70% after MNP internalization inside human adenocarcinoma SKOV-3 cells [13]. This decrease for intracellular MNP can be attributed to a combination of MNP agglomeration effects (inducing particle interactions which influence Néel relaxation) and immobilization effects (changing Brownian relaxation) [14]. A recent study on experimental AC-magnetometry with 11 nm iron oxide MNP and micromagnetic simulation explained the decrease of SAR for intracellular MNP mainly by agglomeration and arising dipole–dipole particle interaction causing demagnetizing effects rather than immobilization effects [46]. Even though we cannot fully exclude agglomerations, in our present study, the TEM images as well as the magnetization measurements indicate that MNP were homogeneously distributed within the hydrogels (Figs. 6 and 7) and therefore particle agglomeration effects were neglected for the interpretation of the heating results. We attribute the reduction in SAR to the inhibition of MNP physical rotation, i. e. immobilization effects on their Brownian relaxation.

Strong AC (alternating current) magnetic fields - such as the one employed here (H_0= 40 kA·m^{-1}) - were shown to significantly influence both relaxation times even for small particles sizes [47]. In the following, we will estimate the respective contribution of Néel and Brownian relaxation to particle heating for the MNP investigated here suspended in water based on relations taken from literature. Our estimations are carried out for the mean hydrodynamic diameter, d_H, and the mean core size, d_C, (reported above in 3.1) neglecting size-distribution effects leading to an effectively broad spectrum of relaxation times. Yoshida and Enpuku derived the following expression from the Fokker-Planck equation the for the AC-field-dependent Brownian relaxation time [48]:

$$\tau_B(H_0) = \frac{\tau_B}{\sqrt{1 + 0.21\cdot\xi(H_0)^2}}, \tag{6}$$

with $\tau_B = 3\eta V_H/(k_B T)$ the field-independent Brownian relaxation time, η the viscosity, $V_H = \pi/6\cdot d_H^3$ the hydrodynamic particle volume, T the temperature and $\xi(H_0) = mH_0/(k_B T)$ the reduced field parameter, where $m = \mu_0 M_S V_C$ is the magnetic particle moment. Equation (6) is valid for $\xi\lesssim$ 20. For our case ξ is approximately 2.

The AC-field dependent Néel relaxation time can be expressed in terms of the anisotropy field $H_K = 2K_{eff}/\mu_0 M_S$ [49]:

$$\tau_N(H_0) = \tau_0\cdot\exp\left(\frac{K_{eff}V_C}{k_B T}\cdot\left(1-\frac{H_0}{H_K}\right)^2\right), \tag{7}$$

with $\tau_N = \tau_0\cdot\exp((K_{eff}V_C)/(k_B T))$ the field-independent Néel relaxation time, $\tau_0 = 10^{-9}$ s the time constant [50] and K_{eff} the effective anisotropy constant. Using Eqs. (6) and (7) and applying the properties for the MNP investigated here (cf. Section 3.1) as well as T= 313 K (the saturation temperature achieved during particle heating; s. Supplementary Material S2) and η=6.53·10^{-4} Pa·s (the viscosity of water), a mean Brownian relaxation time of $\tau_B(H_0$= 40 kA·m^{-1}) = 1.21 µs and a mean Néel relaxation time of $\tau_N(H_0$= 40·kA m^{-1}) = 0.17 µs is calculated. Note that the MNP are dominated by Néel relaxation in ambient conditions. The effective relaxation time

$$\tau_R = \frac{1}{\tau_B^{-1} + \tau_N^{-1}} = \frac{\tau_B}{1 + \frac{\tau_B}{\tau_N}} = \frac{\tau_N}{1 + \frac{\tau_N}{\tau_B}} \tag{8}$$

results in $\tau_R(H_0$= 40 kA·m^{-1}) = 0.15 µs. Using Eq. (8) and knowing that $\tau_B(H_0$= 40 kA·m^{-1})/$\tau_N(H_0$= 40 kA·m^{-1}) ≈ 7.12, we estimate the acceleration of the effective combined Brownian and Néel relaxation compared to the respective isolated effect to $\tau_R \approx 0.12\tau_B(H_0$= 40 kA·m^{-1}) resp. $\tau_R \approx 0.88\tau_N(H_0$= 40 kA m^{-1}). From this, we expect a Néel dominated particle relaxation, however, also showing significant Brownian contributions which explain the decrease in SAR by inhibition of the Brownian rotation. Moreover, the particle heating efficiency is proportional to the imaginary part of the complex AC-susceptibility, reading [49]:

$$\mathrm{SAR} \propto \chi'' = \chi_0\cdot\frac{2\pi\cdot f\cdot\tau}{1 + (2\pi\cdot f\cdot\tau)^2}, \tag{9}$$

with the initial susceptibility χ_0 and the excitation frequency f. According to Eq. (9), the SAR is maximized for $2\pi\cdot f^*\cdot\tau = 1 \Rightarrow f^* = 1/(2\pi\cdot\tau)$, with the resonance frequencies $f^*(\tau_R$= 0.15 µs) ≈ 1,060 kHz, $f^*(\tau_N$= 0.17 µs) ≈ 940 kHz and $f^*(\tau_B$= 1.21 µs) ≈ 130 kHz in our case. In order to estimate the effect of smaller and bigger particles within the size distribution on SAR, we calculated $\chi''(f, \tau)$ for four exemplary particle sizes: d_C, $d_C-\sigma_{d_C}$, $d_C + \sigma_{d_C}$, $d_C + 2\sigma_{d_C}$ (using the

Table 1
MNP properties used for the estimation of $\chi''(f, \tau)$.

Size	d_C [nm]	d_H [nm]	K_{eff} [kJ/m^3]	$\tau_N(H_0)$ [μs]	$\tau_B(H_0)$ [μs]	$\tau_R(H_0)$ [μs]
d_C	8.9	18.9	81	0.170	1.205	0.149
$d_C-\sigma_{d_C}$	7.6	17.6	93	0.046	1.136	0.044
$d_C+\sigma_{d_C}$	10.2	20.2	72	0.735	1.181	0.453
$d_C+2\sigma_{d_C}$	11.5	21.5	65	3.654	1.102	0.847

PDF fitting parameters, s. Appendix 5A). We assumed a fixed coating thickness of 5 nm for the determination of the hydrodynamic diameter, resulting in $d_H = d_C + 10$ nm. The coating thickness is deduced from the mean particle core and hydrodynamic sizes determined from TEM and DLS measurement (cf. Section 3.1). Further, we assumed a size-dependent effective anisotropy constant as follows [51]:

$$K_{eff}(d_C) = K_B + \frac{6}{d_C}\cdot K_S, \tag{10}$$

with the bulk anisotropy value K_B (=11 kJ·m^{-3} for bulk magnetite [52]) and the surface effective anisotropy constant K_S. Using the value K_{eff} determined from the ZFC-FC measurements (cf. Section 3.1), we calculated K_S=103.83 μJ·m^{-2}. For this K_S value, K_{eff} for the above-mentioned exemplary sizes was approximated. The MNP properties and the respective relaxation times used for the estimation of χ'' are listed in Table 1.

Even though the values in Table 1 are approximations, they allow the estimation of $\chi''(f)$ at different particle sizes directly translating to the SAR. For the following interpretation, we assume that $\chi''(\tau_R)$ holds for MNP dispersed in water (allowing both Brownian and Néel relaxation), $\chi''(\tau_N)$ for MNP fully immobilized (allowing only Néel relaxation) and $\chi''(\tau_B)$ for the MNP Brownian relaxation contribution to the effective relaxation. Fig. 9a shows that for the excitation frequency of f=270 kHz and the mean particle size d_C, the curves for $\chi''(\tau_R)$ and $\chi''(\tau_N)$ nearly overlap and therefore not much change in SAR is expected upon particle immobilization as the MNP relaxation is Néel dominated. For smaller-than-average particles (condition $d_C-\sigma_{d_C}$ in Table 1, Fig. 9b), the peak of $\chi''(\tau_N)$ and $\chi''(\tau_R)$ shifts to much higher frequencies indicating that the resonance condition is not met for the excitation frequency used in this work. For such small particles only a small contribution to the overall SAR is expected. These particles are fully Néel dominated and their immobilization would not have any effect on the SAR.

For larger particles within the size distribution (conditions $d_C + \sigma_{d_C}$ and $d_C + 2\sigma_{d_C}$ in Table 1, Fig. 9c and d), two things are observed:

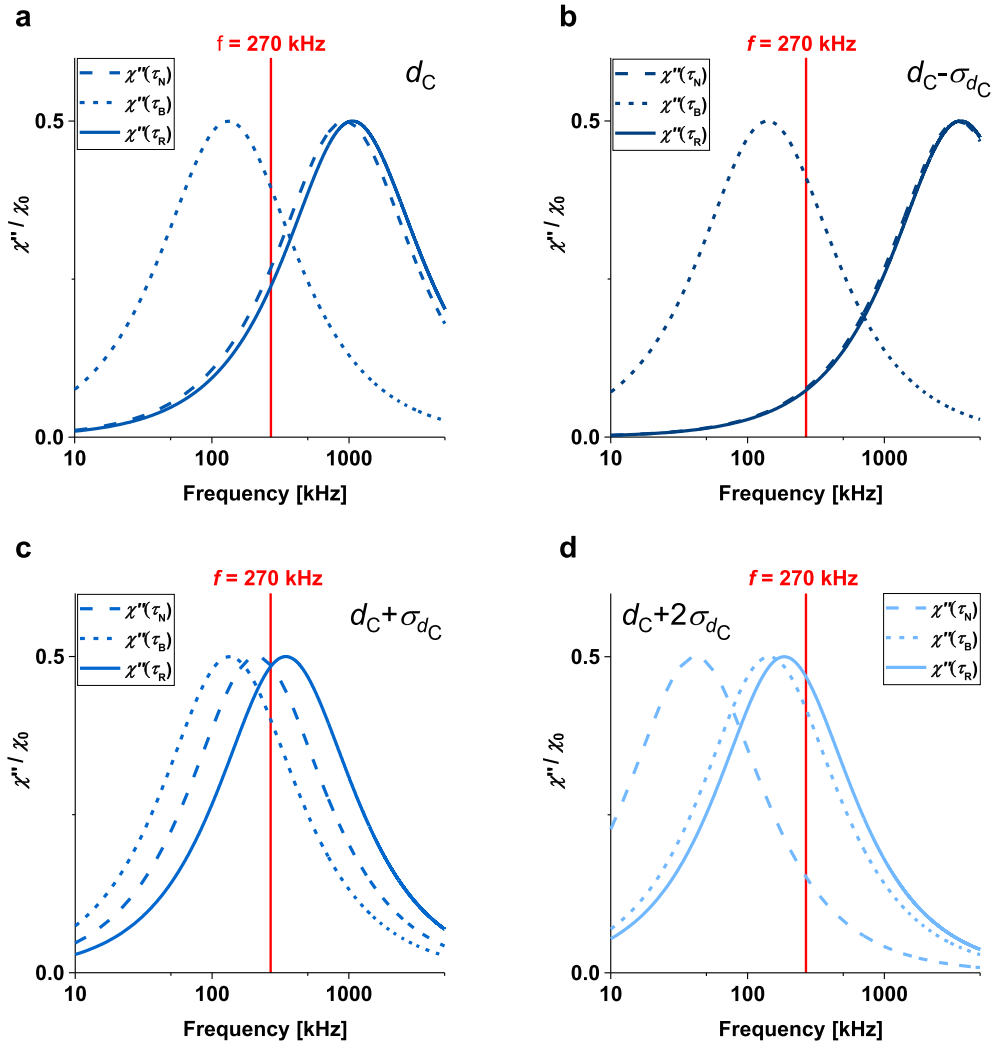

Fig. 9. Imaginary part of the complex AC-susceptibility χ'' (cf. Eq. (9)) versus frequency for different Néel and Brownian relaxation contributions and for the effective relaxation as well as different particle sizes within the size distribution (s. Table 1): (a) mean particle sizes d_C, (b) particles with $d_C-\sigma_{d_C}$, (c) particles with $d_C + \sigma_{d_C}$ and (d) particles with $d_C + 2\sigma_{d_C}$. The excitation frequency used for hyperthermia experiments, f=270 kHz is marked in red. (For interpretation of the references to colour in this figure legend, the reader is referred to the web version of this article.)

Firstly, for higher particle sizes than d_C, the peak in $\chi''(\tau_N)$ shifts rapidly to small frequencies, while $\chi''(\tau_B)$ shifts much closer to $\chi''(\tau_R)$ indicating an increase of Brownian contributions to particle heating (Fig. 9d). Such an effect was reported in literature before [2,53]. Secondly, the resonance condition for $\chi''(f, \tau_R)$ is met and the overall SAR is substantially increased by predominantly Brownian contributions of larger particles. If Brownian relaxation contributions are inhibited by particle immobilization in hydrogels, the contribution of these particles to particle heating is reduced. Even if the absolute number of larger particles is low in the MNP suspension, their Brownian relaxation contributions to the overall SAR value are substantial. This fits to our observation that for the strongest immobilization state, the inhibition of the Brownian relaxation causes a decrease of roughly one third in the MNP heating efficiency.

4. Conclusions

We quantified the drop in heating efficiency for gradual immobilization of MNP inside acrylamide hydrogels. These hydrogels are synthesized with tunable mesh size allowing a continuous inhibition of the Brownian particle relaxation with decreasing mesh size. The highest drop in SAR value of about 35% is measured for MNP with a hydrodynamic size higher than the smallest gel mesh size investigated here. Based on estimations of the field-dependent relaxation time for the MNP used in this work, we conclude that such a decrease in particle heating is caused by a strong inhibition of Brownian relaxation. Consequently, we expect that the Brownian relaxation contributes about 35% to MNP heating, which fits to our conclusion derived from blocking of particle heating in the highest immobilization state and the strongest inhibition of physical particle rotation.

The synthesized hydrogels prove to be an appropriate model for the design of tissue equivalent phantoms. Due to their tunable mesh size, such gel phantoms can be employed to quantify the immobilization effects not only on heating efficiency but also on magnetic resonance and magnetic particle imaging for a variety of MNP with different sizes and surface properties.

Acknowledgements

We thank Dr. Eva Miriam Buhl for assistance with TEM experiments. This work was supported by the German Research Foundation (DFG) within SPP 1681 and is funded as part of the program “Joint Industrial Research (IGF)” by the German Federal Ministry of Economics (contract number: 19735N). U.E. was supported by the German Federal Fellowship Cusanuswerk e.V..

Declaration of interest

None.

Appendix A

A: Log-normal distribution probability density function

The log-normal distribution probability density function (PDF) is defined as

$$\mathrm{PDF}(d, \mu, \sigma) = \frac{1}{\sqrt{2\pi}\cdot d\cdot\sigma}\cdot\exp\left(\frac{(\ln(d)-\mu)^2}{2\sigma^2}\right), \tag{A.1}$$

and the cumulative distribution function (CDF) is defined as

$$\mathrm{CDF}(d, \mu, \sigma) = \frac{1}{2}\left(1 + \mathrm{erf}\left(\frac{\ln(d)-\mu}{\sqrt{2}\,\sigma}\right)\right), \tag{A.2}$$

with the error function, $\mathrm{erf}(x) = 2/\sqrt{\pi}\cdot\int_0^x \exp(-t^2)dt$, and the parameters, μ and σ, from which the mean and variance are calculated with $d_C = \exp(\mu + \sigma^2/2)$ and $\sigma_{dC}^2 = \exp(2\mu + \sigma^2)\cdot(\exp(\sigma^2)-1)$, respectively.

Appendix B. Supplementary material

Supplementary data to this article can be found online at https://doi.org/10.1016/j.jmmm.2018.09.113.

References

[1] Z. Hedayatnasab, F. Abnisa, W.M.A.W. Daud, Review on magnetic nanoparticles for magnetic nanofluid hyperthermia application, Mater. Des. 123 (2017) 174–196.
[2] E.Y.K. Ng, S.D. Kumar, Physical mechanism and modeling of heat generation and transfer in magnetic fluid hyperthermia through Néelian and Brownian relaxation: a review, Biomed. Eng. Online 16 (2017) 36.
[3] C. Blanco-Andujar, F. Teran, D. Ortega, Current outlook and perspectives on nanoparticle-mediated magnetic hyperthermia, Iron Oxide Nanoparticles for Biomedical Applications, Elsevier, 2018, pp. 197–245.
[4] K. Mahmoudi, A. Bouras, D. Bozec, R. Ivkov, C. Hadjipanayis, Magnetic hyperthermia therapy for the treatment of glioblastoma: a review of the therapy’s history, efficacy, and application in humans, Int. J. Hyperther (2018) 1–36.
[5] M. Torres-Lugo, C. Rinaldi, Thermal potentiation of chemotherapy by magnetic nanoparticles, Nanomedicine 8 (2013) 1689–1707.
[6] A. Hervault, N.T.K. Thanh, Magnetic nanoparticle-based therapeutic agents for thermo-chemotherapy treatment of cancer, Nanoscale 6 (2014) 11553–11573.
[7] K. Maier-Hauff, F. Ulrich, D. Nestler, H. Niehoff, P. Wust, B. Thiesen, H. Orawa, V. Budach, A. Jordan, Efficacy and safety of intratumoral thermotherapy using magnetic iron-oxide nanoparticles combined with external beam radiotherapy on patients with recurrent glioblastoma multiforme, J. Neuro-Oncol. 103 (2011) 317–324.
[8] S.V. Spirou, S.A. Costa Lima, P. Bouziotis, S. Vranješ-Djurić, E.K. Efthimiadou, A. Laurenzana, A.I. Barbosa, I. Garcia-Alonso, C. Jones, D. Jankovic, Recommendations for in vitro and in vivo testing of magnetic nanoparticle hyperthermia combined with radiation therapy, Nanomaterials 8 (2018) 306.
[9] M. Johannsen, U. Gneueckow, B. Thiesen, K. Taymoorian, C.H. Cho, N. Waldofner, R. Scholz, A. Jordan, S.A. Loening, P. Wust, Thermotherapy of prostate cancer using magnetic nanoparticles: Feasibility, imaging, and three-dimensional temperature distribution, Eur. Urol. 52 (2007) 1653–1662.
[10] P.S. Yarmolenko, E.J. Moon, C. Landon, A. Manzoor, D.W. Hochman, B.L. Viglianti, M.W. Dewhirst, Thresholds for thermal damage to normal tissues: an update, International journal of hyperthermia : the official journal of European Society for Hyperthermic Oncology, North American Hyperthermia, Group 27 (2011) 320–343.
[11] C. Wilhelm, F. Gazeau, Universal cell labelling with anionic magnetic nanoparticles, Biomaterials 29 (2008) 3161–3174.
[12] N. Oh, J.-H. Park, Endocytosis and exocytosis of nanoparticles in mammalian cells, Int. J. Nanomed. 9 (2014) 51.
[13] R. Di Corato, A. Espinosa, L. Lartigue, M. Tharaud, S. Chat, T. Pellegrino, C. Menager, F. Gazeau, C. Wilhelm, Magnetic hyperthermia efficiency in the cellular environment for different nanoparticle designs, Biomaterials 35 (2014) 6400–6411.
[14] U. Engelmann, A. Roeth, D. Eberbeck, E.M. Buhl, U. Neumann, T. Schmitz-Rode, I. Slabu, Combining bulk temperature and nanoheating enables advanced magnetic fluid hyperthermia efficacy on pancreatic tumor cells, Sci. Rep.-Uk 8 (2018) 13210.
[15] U. Engelmann, E.M. Buhl, M. Baumann, T. Schmitz-Rode, I. Slabu, Agglomeration of magnetic nanoparticles and its effects on magnetic hyperthermia, Curr. Direct. Biomed. Eng. 3 (2017) 457–460.

[16] G. Lamouche, B.F. Kennedy, K.M. Kennedy, C.-E. Bisaillon, A. Curatolo, G. Campbell, V. Pazos, D.D. Sampson, Review of tissue simulating phantoms with controllable optical, mechanical and structural properties for use in optical coherence tomography, Biomed. Opt. Express 3 (2012) 1381–1398.

[17] B.W. Pogue, M.S. Patterson, Review of tissue simulating phantoms for optical spectroscopy, imaging and dosimetry, J. Biomed. Opt. 11 (2006) 041102.

[18] N. Frickel, R. Messing, A.M. Schmidt, Magneto-mechanical coupling in $CoFe_2O_4$-linked PAAm ferrohydrogels, J. Mater. Chem. 21 (2011) 8466–8474.

[19] X. Zhao, J. Kim, C.A. Cezar, N. Huebsch, K. Lee, K. Bouhadir, D.J. Mooney, Active scaffolds for on-demand drug and cell delivery, Proc. Natl. Acad. Sci. 108 (2011) 67–72.

[20] N.N. Reddy, S. Ravindra, N.M. Reddy, V. Rajinikanth, K.M. Raju, V.S. Vallabhapurapu, Temperature responsive hydrogel magnetic nanocomposites for hyperthermia and metal extraction applications, J. Magn. Magn. Mater. 394 (2015) 237–244.

[21] Z.-Q. Zhang, S.-C. Song, Thermosensitive/superparamagnetic iron oxide nanoparticle-loaded nanocapsule hydrogels for multiple cancer hyperthermia, Biomaterials 106 (2016) 13–23.

[22] R. Massart, Preparation of aqueous magnetic liquids in alkaline and acidic media, Ieee T Magn 17 (1981) 1247–1248.

[23] G.L. Béalle, R. Di Corato, J. Kolosnjaj-Tabi, V. Dupuis, O. Clément, F. Gazeau, C. Wilhelm, C. Ménager, Ultra magnetic liposomes for MR imaging, targeting, and hyperthermia, Langmuir 28 (2012) 11834–11842.

[24] R. Brewster, Paint .NET-Free Software for Digital Photo Editing, Getpaint. net. Ultimo acceso, 15 (2017).

[25] R.R. Wildeboer, P. Southern, Q.A. Pankhurst, On the reliable measurement of specific absorption rates and intrinsic loss parameters in magnetic hyperthermia materials, J. Phys. D-Appl. Phys. 47 (2014).

[26] T.J. Ahrens, Rock Physics and Phase Relations: A Handbook of Physical Constants, American Geophysical Union, 1995.

[27] S. Pal, P. Dutta, N. Shah, G.P. Huffman, M.S. Seehra, Surface spin disorder in Fe_3O_4 nanoparticles probed by electron magnetic resonance spectroscopy and magnetometry: Ieee Transactions on Magnetics, IEEE Trans. Magn. 43 (2007) 3091–3093.

[28] C. Schmitz-Antoniak, D. Schmitz, A. Warland, M. Darbandi, S. Haldar, S. Bhandary, B. Sanyal, O. Eriksson, H. Wende, Suppression of the verwey transition by charge trapping, Annalen der Physik 530 (2018) 1700363.

[29] B.D. Cullity, C.D. Graham, Introduction to Magnetic Materials, John Wiley & Sons, 2011.

[30] L. Roeder, M. Reckenthäler, L. Belkoura, S. Roitsch, R. Strey, A. Schmidt, Covalent ferrohydrogels based on elongated particulate cross-linkers, Macromolecules 47 (2014) 7200–7207.

[31] D. Calvet, J.Y. Wong, S. Giasson, Rheological monitoring of polyacrylamide gelation: Importance of cross-link density and temperature, Macromolecules 37 (2004) 7762–7771.

[32] J.E. Mark, Physical Properties of Polymers Handbook, Springer, 2007.

[33] L. Treloar, Physics of Rubber Elasticity (Oxford classic texts in the physical sciences), Oxford University Press, 2005.

[34] A. Chrambach, D. Rodbard, Polyacrylamide gel electrophoresis, Science 172 (1971) 440–451.

[35] J. Wang, V.M. Ugaz, Using in situ rheology to characterize the microstructure in photopolymerized polyacrylamide gels for DNA electrophoresis, Electrophoresis 27 (2006) 3349–3358.

[36] M.A. Martens, R.J. Deissler, Y. Wu, L. Bauer, Z. Yao, R. Brown, M. Griswold, Modeling the Brownian relaxation of nanoparticle ferrofluids: Comparison with experiment, Med. Phys. 40 (2013).

[37] F.B. Wyart, P.-G. de Gennes, Viscosity at small scales in polymer melts, Eur. Phys. J. E 1 (2000) 93–97.

[38] T. Ge, J.T. Kalathi, J.D. Halverson, G.S. Grest, M. Rubinstein, Nanoparticle motion in entangled melts of linear and nonconcatenated ring polymers, Macromolecules 50 (2017) 1749–1754.

[39] E. Roeben, L. Roeder, S. Teusch, M. Effertz, U.K. Deiters, A.M. Schmidt, Magnetic particle nanorheology, Colloid Polym. Sci. 292 (2014) 2013–2023.

[40] M. Hermes, E. Roeben, L. Kibkalo, A.M. Schmidt, Magnetic particle nanorheology in complex fluids, Annu. Trans. Nord. Rheol. Soc. 25 (2017) 97–105.

[41] L.-H. Cai, S. Panyukov, M. Rubinstein, Mobility of nonsticky nanoparticles in polymer liquids, Macromolecules 44 (2011) 7853–7863.

[42] M. Bohdanecký, V. Petrus, B. Sedláček, Estimation of the characteristic ratio of polyacrylamide in water and in a mixed theta-solvent, Die Makromolekulare Chem. 184 (1983) 2061–2073.

[43] D. Cabrera, A. Lak, T. Yoshida, M. Materia, D. Ortega, F. Ludwig, P. Guardia, A. Sathya, T. Pellegrino, F. Teran, Unraveling viscosity effects on the hysteresis losses of magnetic nanocubes, Nanoscale 9 (2017) 5094–5101.

[44] R. Ludwig, M. Stapf, S. Dutz, R. Müller, U. Teichgräber, I. Hilger, Structural properties of magnetic nanoparticles determine their heating behavior-an estimation of the in vivo heating potential, Nanoscale Res. Lett. 9 (2014) 602.

[45] D. Soukup, S. Moise, E. Cespedes, J. Dobson, N.D. Telling, In situ measurement of magnetization relaxation of internalized nanoparticles in live cells, ACS Nano 9 (2015) 231–240.

[46] D. Cabrera, A. Coene, J. Leliaert, E.J. Artes-Ibanez, L. Dupre, N.D. Telling, F.J. Teran, Dynamical magnetic response of iron oxide nanoparticles inside live cells, ACS nano 12 (2018) 2741–2752.

[47] J. Dieckhoff, D. Eberbeck, M. Schilling, F. Ludwig, Magnetic-field dependence of Brownian and Néel relaxation times, J. Appl. Phys. 119 (2016) 043903.

[48] T. Yoshida, K. Enpuku, Simulation and quantitative clarification of AC susceptibility of magnetic fluid in nonlinear Brownian relaxation region, Jpn. J. Appl. Phys. 48 (2009) 127002.

[49] K.M. Krishnan, Fundamentals and Applications of Magnetic Materials, Oxford University Press, 2016.

[50] P. Fannin, S. Charles, On the calculation of the Neel relaxation time in uniaxial single-domain ferromagnetic particles, J. Phys. D Appl. Phys. 27 (1994) 185.

[51] F. Bødker, S. Mørup, S. Linderoth, Surface effects in metallic iron nanoparticles, Phys. Rev. Lett. 72 (1994) 282.

[52] L. Bickford, J. Brownlow, R. Penoyer, Magnetocrystalline anisotropy in cobalt-substituted magnetite single crystals, Proc IEE-Part B: Radio Electron. Eng. 104 (1957) 238–244.

[53] J. Carrey, B. Mehdaoui, M. Respaud, Simple models for dynamic hysteresis loop calculations of magnetic single-domain nanoparticles: Application to magnetic hyperthermia optimization, J. Appl. Phys. 109 (2011) 083921.